

P91 钢焊接接头 IV 型裂纹力学控制参量有限元模拟

张建强^{1,2}, 罗传红², 章应霖²

(1. 哈尔滨工业大学 先进焊接与连接国家重点实验室, 哈尔滨 150001;
2. 武汉大学 动力与机械学院, 武汉 430072)

摘 要: 采用有限元方法对马氏体耐热钢(P91)焊接接头在温度为 600 °C、应力为 80 MPa 下的最大主应力、von Mises 等效应力、等效蠕变应变和应力三轴度进行了数值模拟。结果表明,在接头上下坡口交界处细晶热影响区(FGHAZ)两侧的最大主应力和 von Mises 等效应力很高,蠕变变形主要集中在 FGHAZ,等效蠕变应变的最大值位于 FGHAZ 的底部。受焊缝和母材的强烈拘束,上下坡口交界处 FGHAZ 内应力三轴度最大,容易形成蠕变裂纹,导致接头蠕变开裂。数值模拟结果与试验获得的 IV 型裂纹产生、扩展结果一致。因此采用应力三轴度表征 IV 型裂纹开裂比较合理。

关键词: 马氏体耐热钢; IV 型裂纹; 等效应力; 等效蠕变应变; 数值模拟

中图分类号: TG407 文献标识码: A 文章编号: 0253-360X(2012)03-0057-04



张建强

0 序 言

马氏体耐热钢 P91(9Cr1MoVNb) 具有优良的高温强度、韧性、焊接性、抗氧化及抗热疲劳性能,且易于加工成形。目前已被广泛应用于电力、锅炉、压力容器、石油化工、核电等部门。在火力发电厂,P91 主要被用于超临界机组主蒸汽管道^[1,2]。长期服役过程中,接头的细晶热影响区(FGHAZ)会产生 IV 型蠕变裂纹,导致接头发生早期蠕变失效,从而引起人们广泛关注^[3,4]。

IV 型裂纹蠕变失效主要发生在铁素体类耐热钢焊接接头中。从 20 世纪 70 年代以来,人们便开始了广泛研究,但主要限于含 Cr 元素低的耐热钢,对 IV 型蠕变失效的许多方面仍缺乏系统了解^[5]。P91 钢接头的 IV 型蠕变失效与含 Cr 元素低的接头不同,其失效的力学机理比较复杂。关于 IV 型裂纹产生的力学控制参量认识不一,迄今尚未形成统一的观点。给问题的分析、IV 型裂纹的控制以及 P91 接头的蠕变寿命预测带来很大困难。Tabuchi 等人^[3]采用试验测量、有限元方法对 P91 钢焊接接头的组织和蠕变损伤进行了研究。Watanabe 等人^[4]采用长期蠕变断裂试验,研究了 P91 钢接头的蠕变断裂性能和微观组织。

文中以马氏体耐热钢 P91 焊接接头为对象,采用焊缝、细晶区、母材三材料模型(高温 HAZ 归入焊缝)利用大型商用软件对接头在温度为 600 °C、应力为 80 MPa 下的蠕变最大主应力、von Mises 等效应力、等效蠕变应变、应力三轴度等进行有限元模拟。特别是 FGHAZ 及附近区域的情况进行详尽分析。探讨接头在运行过程中最大主应力、von Mises 等效应力、等效蠕变应变和应力三轴度分布及变化特征,提出 IV 型裂纹开裂的力学控制参量,为合理选择焊接材料、制订焊接工艺,防止接头早期 IV 型蠕变失效打下坚实基础。

1 计算模型

1.1 试验材料和接头形式

试验材料为马氏体耐热钢 P91,焊缝填充材料为 TGS-9cb,母材和焊丝的化学成分如表 1 所示。

表 1 母材和焊丝的化学成分(质量分数,%)

Table 1 Chemical compositions of base metals and filler metals

材料	C	Si	Mn	S	P	Cr
P91 母材	0.01	0.40	0.46	0.010	0.010	8.85
TGS-9cb 焊丝	0.07	0.16	0.099	0.008	0.006	8.97
材料	Mo	V	Nb	Ni	Al	N
P91 母材	0.93	0.21	0.09	0.01	0.003	0.038
TGS-9cb 焊丝	0.90	0.18	0.10	0.68	—	—

收稿日期: 2011-10-24

基金项目: 先进焊接与连接国家重点实验室开放课题; 湖北省自然科学基金资助项目(2007ABA040)

1.2 焊接工艺及持久试验

采用焊条氩弧焊接工艺,坡口形式为双V形对接,根部V形坡口面角度为 30° ,无钝边,上部V形坡口面角度为 5° 。焊完经机械加工后模型的根部焊道与混合HAZ宽度之和为9 mm,FGHAZ的宽度为1.0 mm。采用多层多道焊接,每层焊接工艺参数相同,焊接电流为200 A,电弧电压为11 V,焊接速度为100 mm/min,焊接第1、2层背面充氩气保护,气体流量为10 L/min,焊前预热温度为 $150 \sim 200^\circ\text{C}$,层间温度为 $150 \sim 200^\circ\text{C}$,焊后热处理为 $743^\circ\text{C} \times 8.5 \text{ h}$ [3]。

1.3 网格划分

取试样的1/2进行建模,模型的形状与尺寸如图1所示。FGHAZ网格较密,网格尺寸为 $0.1 \text{ mm} \times 0.36 \text{ mm} \times 1 \text{ mm}$ (分别为 x, y, z 方向尺寸),然后逐步加粗,远离FGHAZ区域的试件边缘的网格尺寸最大,为 $1.06 \text{ mm} \times 0.6 \text{ mm} \times 1 \text{ mm}$,厚度方向分5层,模型的节点数为20 202,单元数为16 200,网格划分如图2所示。

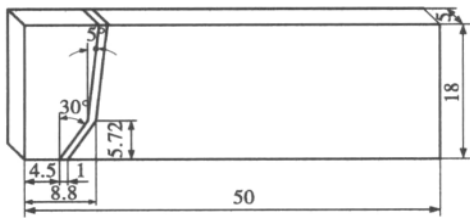


图1 有限元模型的形状及尺寸(mm)
Fig. 1 Figuration and sizes of FEM model

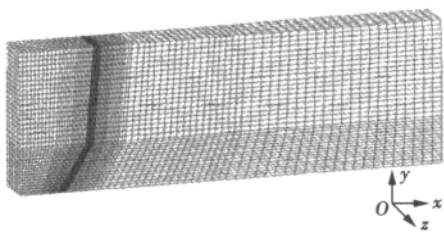


图2 有限元网格划分
Fig. 2 Meshing scheme

1.4 边界条件

为了防止试样在蠕变计算过程中产生平移或转动,但又不至于影响模拟计算结果,将模型左端节点 x, y, z 和右端节点 y, z 方向位移进行约束。外载荷以面应力的形式作用于试样的右端,为80 MPa,模拟蠕变时间为20 000 h。

1.5 材料本构关系

采用Bailey-Norton定律描述蠕变过程,最小蠕变应变变速率与施加的轴向拉应力关系式为

$$\dot{\varepsilon}^C = A\sigma^n \quad (1)$$

式中: A, n 分别为给定温度下的蠕变系数和蠕变指数; $\dot{\varepsilon}^C$ 为最小蠕变应变变速率; σ 为施加的轴向拉应力。材料的力学性能和蠕变参数如表2所示 [3, 4]。

表2 600 °C时材料力学性能和蠕变参数

Table 2 Mechanical properties and creep parameters of materials at 600 °C

材料	屈服强度 R_{eL}/MPa	弹性模量 E/GPa	蠕变系数 A	蠕变指数 n
P91 母材	458.0	109	4.94×10^{-29}	11.1
FGHAZ	382.8	109	4.53×10^{-21}	7.8
焊缝	478.0	109	7.20×10^{-25}	8.6

2 数值模拟结果

2.1 最大主应力模拟结果

金属材料的蠕变失效是晶界孔洞形核及孔洞扩展的结果,而蠕变孔洞形核受最大主应力控制。外加轴向应力80 MPa作用下,模拟12 111 h 时间后FGHAZ附近的最大主应力分布如图3所示。由图3可知,最大主应力位于混合HAZ,且靠近上侧V形坡口与FGHAZ交界附近的混合HAZ,而FGHAZ内的最大主应力数值不大。由图3b可以看出,上下V形坡口交界处($y = 5.72 \text{ mm}$)最大主应力的峰值位于 $x = 7.6 \text{ mm}$ 位置,数值为89.7 MPa。而混合HAZ和FGHAZ交界处($x = 7.8 \text{ mm}$)的最大主应力为87.2 MPa。FGHAZ内靠近T91母材外侧($x = 8.4 \text{ mm}$)的最大主应力最小,仅为69.5 MPa。因此,如果按最大主应力控制蠕变失效准则分析FGHAZ内IV型蠕变裂纹形核、扩展特性,显然与试验结果不吻合。

2.2 von Mises 等效应力

在外加轴向应力80 MPa作用下,模拟12 111 h后von Mises等效应力分布如图4所示。由图4可知,最大von Mises等效应力位于混合HAZ中,靠近上V形坡口的FGHAZ,而FGHAZ内以及与FGHAZ相邻的母材中的von Mises等效应力数值不大。根据图4b,沿上下V形坡口交界处最大von Mises等效应力位于 $x = 7.6 \text{ mm}$ 处,数值为95.8 MPa。而混合HAZ和FGHAZ交界处($x = 7.8 \text{ mm}$)的von Mises等效应力为77.7 MPa。靠近母材一侧FGHAZ中的von Mises等效应力较小, $x = 8.1 \sim 8.4 \text{ mm}$ 区域内,

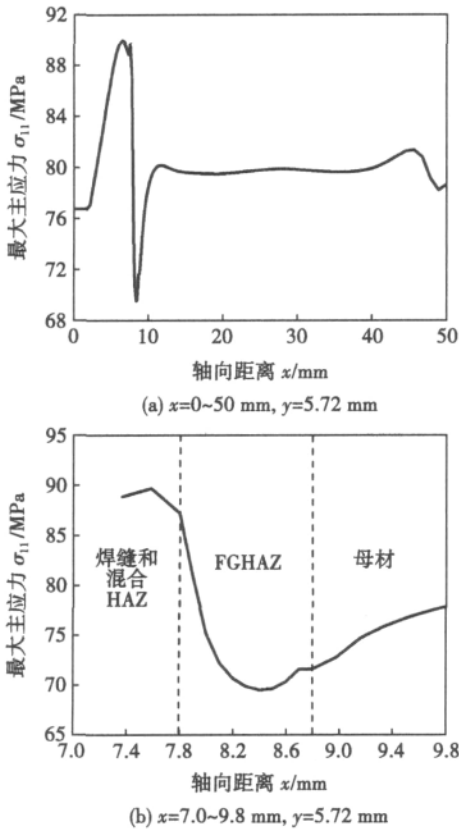


图 3 最大主应力沿试样长度方向分布
Fig. 3 Distributions of maximum principal stress along longitudinal direction of specimen

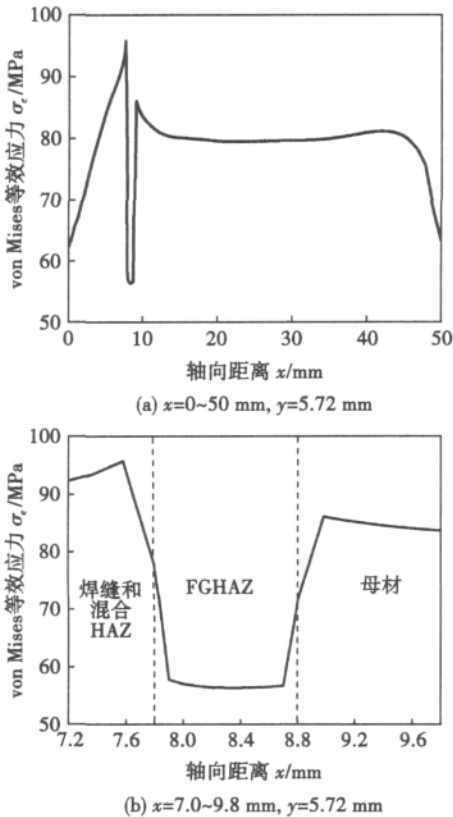


图 4 细晶区附近 von Mises 等效应力分布
Fig. 4 Distributions of von Mises equivalent stress longitudinal direction of specimen near fine grain region

von Mises 等效应力约为 56 MPa. 如果按 von Mises 等效应力控制蠕变失效准则分析 FGHAZ 内 IV 型裂纹形核、扩展特性, 也与试验结果不相符.

2.3 等效蠕变应变

在 80 MPa 应力作用下, 模拟 12 111 h 后等效蠕变应变沿试样长度方向的分布如图 5 所示.

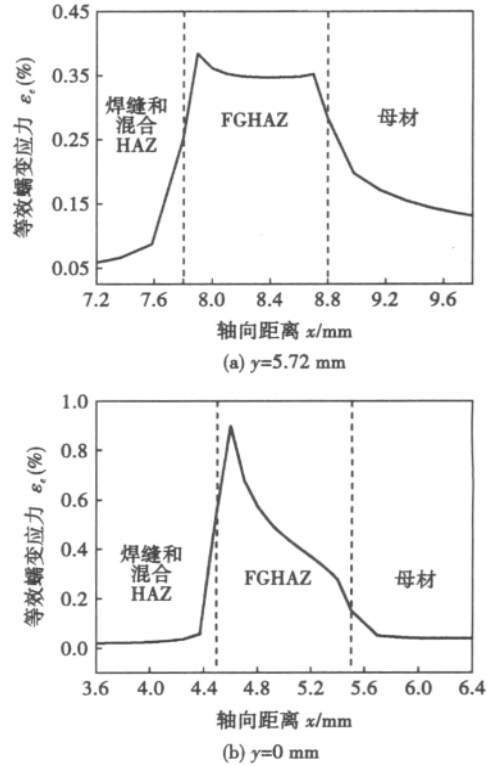


图 5 $y=5.72$ mm 和 $y=0$ mm 细晶区附近等效蠕变应变分布

Fig. 5 Distributions of equivalent creep strain near fine grain region ($y=5.72$ mm and $y=0$ mm)

由图 5 可知, 最大等效蠕变应变位于下 V 形坡口底部 FGHAZ 内, 且靠近混合 HAZ 附近区域 ($x=4.6$ mm, $y=0$ mm), 数值为 8.984×10^{-3} , 而上下坡口交界处 FGHAZ ($x=7.9$ mm, $y=5.72$ mm) 内的等效蠕变应变为 3.846×10^{-3} . 根据蠕变韧性耗竭理论, 下 V 形坡口 FGHAZ 蠕变损伤最大, 蠕变孔洞应优先在该区域形核、长大、形成蠕变裂纹. 根据试验结果和文献 [5, 6] 报道, 蠕变孔洞在上下 V 形坡口交界部位的 FGHAZ 内优先形核、长大、最终形成蠕变裂纹导致接头失效. 由此可见, 采用等效蠕变应变进行蠕变损伤和断裂评定 P91 钢 IV 型开裂与试验不吻合. 采用基于蠕变韧性耗竭方法对具有 IV 型裂纹倾向的焊接接头进行寿命评估难以获得准确结果, 因而不适用.

2.4 应力三轴度

应力三轴度因子 R_σ 定义为

$$R_\sigma = \frac{\sigma_m}{\sigma_e} \quad (2)$$

$$\sigma_m = \frac{1}{3}(\sigma_1 + \sigma_2 + \sigma_3) \quad (3)$$

$$\sigma_e = \frac{\sqrt{2}}{2} [(\sigma_1 - \sigma_2)^2 + (\sigma_2 - \sigma_3)^2 + (\sigma_3 - \sigma_1)^2]^{\frac{1}{2}} \quad (4)$$

式中: σ_1 σ_2 σ_3 为第一、第二、第三主应力; σ_m 为平均应力; σ_e 为 von Mises 等效应力。

在轴向应力 80 MPa 作用下 模拟运行 12 111 h 后 $x=5 \sim 10$ mm 应力三轴度因子 R_σ 沿试样长度方向的分布如图 6 所示。

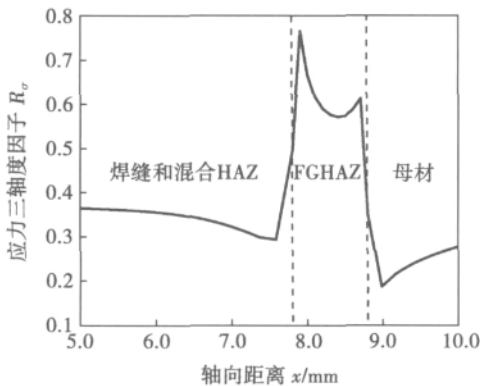


图 6 应力三轴度因子沿试样长度方向分布

Fig. 6 Distributions of stress triaxiality along longitudinal direction

由图 6 可知, 应力三轴度因子 R_σ 在 $x=5 \sim 10$ mm 范围内分布不均匀。原因是 FGHAZ 两侧材料的蠕变强度高, 对 FGHAZ 产生强烈约束, 使 FGHAZ 处于三轴应力状态。FGHAZ 内 R_σ 值高于焊缝 + 混合 HAZ 和母材中的应力三轴度因子。 R_σ 在 FGHAZ 内存在两个峰值, 最大值为 0.77, 位于 $x=7.9$ mm, 即靠近混合 HAZ 的 FGHAZ 内。另一个峰值位于临近母材 FGHAZ 内, 即 $x=8.7$ mm 处, 此时 $R_\sigma=0.61$ 。而 FGHAZ 中间部位的 R_σ 也较高, $x=8 \sim 8.6$ mm 时 $R_\sigma=0.57 \sim 0.67$ 。靠近 P91 母材 FGHAZ 中的应力三轴度因子低于临近混合 HAZ 一侧 FGHAZ 中的应力三轴度因子, 主要因为焊缝 + 混合 HAZ 的约束大于母材对 FGHAZ 的约束。而焊缝 + 混合 HAZ 内 R_σ 的最大值为 0.37, 母材区内的 R_σ 的最大值为 0.27。由此可见, 采用应力三轴度准则分析 P91 钢接头 FGHAZ 内蠕变孔洞扩张及 IV 型裂纹扩展特性, 则与试验观察结果吻合较好, 因此以应力三

轴度作为 IV 型裂纹的力学控制判据比较合适。

3 持久试验

为了验证数值模拟结果, 进行了持久试验。试样尺寸为 $100 \text{ mm} \times 17.5 \text{ mm} \times 5 \text{ mm}$, 温度为 $600 \text{ }^\circ\text{C}$, 轴向应力为 80 MPa, 试验时间为 12 000 h。经过 12 000 h 持久试验后, 在 P91 钢 FGHAZ 内发生了蠕变开裂, 如图 7 所示。由图 7 可以看出, 裂纹在上下坡口交界部位及接近上表面的 FGHAZ 内形成、扩展, 为典型 IV 型蠕变裂纹, 试验结果与模拟结果吻合较好。

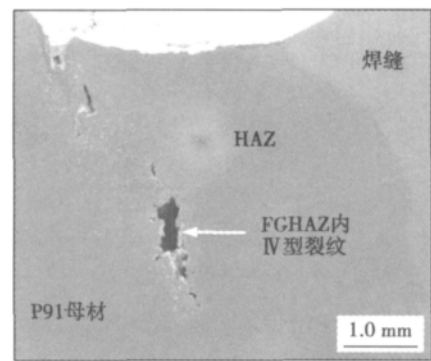


图 7 FGHAZ 区 IV 型蠕变裂纹形貌

Fig. 7 Appearance of type IV crack in FGHAZ

4 结 论

(1) 最大主应力位于靠近上侧 V 形坡口与 FGHAZ 交界附近的混合 HAZ 内, 而 FGHAZ 内的最大主应力数值不大。

(2) 最大 von Mises 等效应力同样位于上 V 形坡口 FGHAZ 内侧的混合 HAZ 中, 而 FGHAZ 内以及与 FGHAZ 相邻的母材区域中的 von Mises 等效应力数值较小。

(3) 最大等效蠕变应变位于下 V 形坡口底部 FGHAZ 靠近混合 HAZ 附近区域, 数值为 8.984×10^{-3} , 而上下坡口交界处的等效蠕变应变为 3.846×10^{-3} 。采用等效蠕变应变评定 P91 钢 IV 型开裂与试验结果不吻合, 因而不能采用蠕变应变方法评估具有 IV 型裂纹倾向的焊接接头的蠕变寿命。

(4) FGHAZ 内应力三轴度因子最大, 存在两个峰值, 最大值位于靠近混合 HAZ 的 FGHAZ 内, 另一个峰值位于 FGHAZ 与母材交界的 FGHAZ 内, 而

[下转第 64 页]

- Song Sili, Wang Xinhong, Zou Zengda. Study on the microstructure and mechanical properties of TiC/Fe composites coating layer [J]. Journal of Shandong University (Engineering Science), 2009, 34(2): 1-5.
- [4] 郭永强, 孙荣禄, 雷贻文, 等. 激光熔覆原位自生 TiC 颗粒增强 Ni 基复合涂层的组织与性能 [J]. 材料热处理学报, 2004, 12(4): 178-181.
- Guo Yongqiang, Sun Ronglu, Lei Yiwen, *et al.* Microstructure and properties of in situ formed TiC particle reinforced Ni-base composite coating by laser cladding [J]. Transactions of Materials and Heat Treatment, 2004, 12(4): 178-181.
- [5] 王新洪, 张敏, 邹增大, 等. 激光熔覆 TiC_p/Ni 基合金复合涂层的显微组织与性能 [J]. 机械工程学报, 2003, 39(2): 37-41.
- Wang Xinhong, Zhang Min, Zou Zengda, *et al.* Micro-structure and properties of laser clad TiCp/Ni-based alloys composite coating [J]. Chinese Journal of Mechanical Engineering, 2003, 39(2): 37-41.
- [6] 张现虎, 晁明举, 梁二军, 等. 激光熔覆原位生成 TiC-ZrC 颗粒增强镍基复合涂层 [J]. 中国激光, 2009, 36(4): 998-1003.
- Zhang Xianhu, Chao Mingju, Liang Erjun, *et al.* In-situ synthesis of TiC-ZrC particulate reinforced Ni-based composite coatings by laser cladding [J]. Chinese Journal of Lasers, 2009, 36(4): 998-1003.

作者简介: 王永东, 男, 1979 年出生, 博士, 副教授. 研究方向为材料表面改性. 发表论文 20 余篇. Email: wyd04@163.com

[上接第 60 页]

FGHAZ 中的应力三轴度因子也较高, 试验结果与模拟结果一致. 采用应力三轴度作为 IV 型裂纹开裂判据和寿命评定的力学参量较为合适.

参考文献:

- [1] Swindemana R W, Santellaa M L, Maziasza P J, *et al.* International Issues in replacing Cr-Mo steels and stainless steels with 9Cr-1Mo-V steel [J]. Journal of Pressure Vessels and Piping, 2004, 81(6): 507-512.
- [2] 杨富, 章应霖, 任永宁, 等. 新型耐热钢焊接 [M]. 北京: 中国电力工业出版社, 2006.
- [3] Tabuchi M, Hongo H, Li Y, *et al.* Evaluation of microstructures and creep damages in the HAZ of P91 steel weldment [J]. Journal of Pressure Vessel Technology, 2009, 131(2): 021406-1-021406-6.
- [4] Watanabe T, Tabuchi M, Yamazaki M, *et al.* Creep damage evaluation of 9Cr-Mo-V-Nb steel welded joints showing type IV fracture [J]. International Journal of Pressure Vessels and Piping, 2006, 83(1): 63-71.
- [5] Perrin I J, Hayhurst D R. Continuum damage mechanics analyses of type IV creep failure in ferritic steel crossweld specimens [J]. International Journal of Pressure Vessels and Piping, 1999, 76(9): 599-617.

作者简介: 张建强, 男, 1964 年出生, 博士, 副教授. 主要从事焊接结构强度与断裂、异种钢焊接、焊接过程数值模拟等方面的教学和科研工作. 发表论文 100 余篇. Email: zhangjq123456@163.com

FEM simulation of mechanical controlling parameters for type IV cracking on P91 steel weld ZHANG Jianqiang^{1,2}, LUO Changhong², ZHANG Yinglin² (1. State Key Laboratory of Advanced Welding and Joining, Harbin Institute of Technology, Harbin 150001, China; 2. School of Power and Mechanical Engineering, Wuhan University, Wuhan 430072, China). pp 57 – 60, 64

Abstract: The maximum principal stress, von Mises equivalent stress and equivalent creep strain of the welded joint of martensitic heat-resistant steel (P91) was simulated by FEM under the condition of 600 °C and 80 MPa. The results show that the maximum principal stress and von Mises equivalent stress are high on the curved points of two sides of groove faces near the fine grain HAZ. The creep strain mainly concentrates in the fine grain HAZ, the maximum creep strain locates in the bottom of fine grain HAZ of the specimen. The stress triaxiality is maximum in the fine grain HAZ and creep cracking occurs because of the intensive constrain of the base metal and weld. The simulation results are in well agreement with the experimental results of crack initiation site and propagation path by using the stress triaxiality as the mechanically controlling parameter of the martensitic heat-resistant steel weld. Therefore, it is reasonable for the stress triaxiality to be used for analyzing the initiation and propagation of type IV cracking in the fine grain HAZ.

Key words: martensitic heat-resistant steel, type IV cracking; von Mises equivalent stress; equivalent creep strain; numerical simulation

Microstructure and wear resistance of (Ti, Nb) C reinforced composite coating in-situ synthesized by argon arc cladding

WANG Yongdong, LI Bairu, WANG Shuhua, LIU Xing (Department of Material Science and Technology, Heilongjiang Institute of Science and Technology, Harbin 150022, China). pp 61 – 64

Abstract: Ni-based reinforced composite coating was prepared on the surface of 16Mn steel by means of argon arc cladding technique with the pre-alloyed powders of Ni60A, Nb, Ti and C. The microstructure of the composite coating was examined with OM, SEM and XRD, and the abrasion property of the coating was measured under different loads. The results showed that metallurgical bonding between the coating and the substrate occurred without defects like pores and cracks. The microstructure of the composite coating consisted of (Ti, Nb) C particles, γ -Ni austenite dendrites and Cr₂₃C₆ eutectics. With the increase of load at room temperature, the weight loss during abrasion of the composite coating increased slowly, whereas that of 16Mn steel increased remarkably. The wear resistance of the composite coating was 11 times higher than that of the substrate.

Key words: argon arc cladding; composite coating; in-situ synthesis; wear resistance

Analysis on microstructure of in-situ synthesis TiC-M₇C₃ ceramic hard phase

LIU Zhengjun, LI Lecheng, ZONG Lin, SU Yunhai (School of Materials Science and Engineering, Shenyang University of Technology, Shenyang 110870, China). pp 65 – 68

Abstract: TiC-M₇C₃ ceramic hard phases were in situ

synthesized using plasma arc surfacing technology. The morphology and distribution of TiC-M₇C₃ hard phases in the surfacing layer was investigated with the X-ray diffraction (XRD), optical microscope (OM), scanning electron microscope (SEM) and spectrum analyzer (EDS). Rockwell hardness tester and wet sand abrasion tester were used to examine the performance of the surfacing layer. The results show that the microstructure of the surfacing layer consists of high-carbon martensite and a large number of ceramic hard phases, for example, TiC and M₇C₃, which disperse in the matrix of surfacing layer. The hardness of the surfacing layer is 66.4 HRC and the weight reduction is 0.086 g. TiC can act as the nuclei of M₇C₃ to improve the nucleation rate of M₇C₃ ceramic hard phases and grain refinement. The Fe-Cr-Ti-C surfacing layer has higher hardness and better wear resistance than Fe-Cr-C alloy due to the combined effect of TiC and M₇C₃ ceramic hard phases.

Key words: ceramic hard phase; surfacing layer; in-situ synthesis; wear resistance

Effects of pulse frequency on TCGMAW droplet transfer modes

XIE Shengmian^{1,2}, WU Kaiyuan¹, WEN Yuanmei^{1,3}, GE Weiqing¹, HUANG Shisheng¹ (1. School of Mechanical & Automotive Engineering, South China University of Technology, Guangzhou 510641, China; 2. School of Information and Communication Engineering, Guangzhou Maritime College, Guangzhou 510725, China; 3. Information Engineering College, Guangdong University of Technology, Guangzhou 510006, China). pp 69 – 72

Abstract: The effects of pulse frequency on TCGMAW (Twin-wire Co-pool Gas-shielded Metal Arc Welding) droplet transfer modes and weld appearances were investigated with high-speed photography and wavelet analysis. Under the welding parameters in this paper, the droplet transfer mode of the front wire was spray transfer and that of the back wire was projected transfer when the pulse frequency was high (140 Hz); the droplet transfer mode of both the front and back wires was projected transfer when the pulse frequency was low (40 Hz); the droplet transfer mode of both the front and back wires was spray transfer when the pulse frequency was moderate (60 – 100 Hz); the droplet transfer of both the front and back wires was one-droplet-per-pulse when the pulse frequency changed between 40 Hz and 140 Hz; and the weld appearances were preferable when the pulse frequency changed between 60 Hz and 100 Hz.

Key words: TCGMAW; droplet transfer; high-speed photography; wavelet analysis; weld appearance

Microstructure transformation of coarse-grained region in heat-affected zone during welding of ultra-low carbon ultra-high strength pipeline steel

LEI Xuanwei¹, WANG Honghong¹, YIN Yuqun², ZHAO Jinbin², QIAN Yong^{1,3}, WU Kaiming¹ (1. International Research Institute for Steel Technology, Wuhan University of Science and Technology, Wuhan 430081, China; 2. Nanjing Iron & Steel Group Co., Ltd., Nanjing 210035, China; 3. Julong Steel Pipe Co., Ltd., Nanjing 210035, China). pp 73 – 76

Abstract: The microstructure transformation of coarse-grained region in heat-affected zone (CG-HAZ) during welding